Nano Research Energy

ISSN 2791-0091 (print); 2790-8119 (online)
https://doi.org/10.26599/NRE.2022.9120033

Research Article

In-situ grown CuO_x nanowire forest on copper foam: A 3D hierarchical and freestanding electrocatalyst with enhanced carbonaceous product selectivity in CO_2 reduction

Wenjun Zhang[1,2], Minghang Jiang[1,3,4], Songyuan Yang[1,3,4], Yi Hu[1,3,4], Bin Mu[5] (✉) Zuoxiu Tie[1,3,4] (✉), and Zhong Jin[1,3,4] (✉)

[1] *MOE Key Laboratory of Mesoscopic Chemistry, MOE Key Laboratory of High Performance Polymer Materials and Technology, Jiangsu Key Laboratory of Advanced Organic Materials, School of Chemistry and Chemical Engineering, Nanjing University, Nanjing 210023, China*
[2] *Jiangsu Co-Innovation Center of Efficient Processing and Utilization of Forest Resources, International Innovation Center for Forest Chemicals and Materials, College of Chemical Engineering, Nanjing Forestry University, Nanjing 210037, China*
[3] *Nanjing Tieming Energy Technology Co. Ltd., Nanjing 210093, China*
[4] *Suzhou Tierui New Energy Technology Co. Ltd., Suzhou 215228, China*
[5] *School for Engineering of Matter, Transport, and Energy, Arizona State University, 501 East Tyler Mall, Tempe, AZ 85287, USA*

Received: 3 March 2022 / **Revised**: 6 May 2022 / **Accepted**: 9 May 2022

ABSTRACT

Electrocatalytic carbon dioxide (CO_2) reduction is considered as an economical and environmentally friendly approach to neutralizing and recycling greenhouse gas CO_2. However, the design of preeminent and robust electrocatalysts for CO_2 electroreduction is still challenging. Herein, we report the *in-situ* growth of dense CuO_x nanowire forest on 3D porous Cu foam (CuO_x-NWF@Cu-F), which can be directly applied as a freestanding and binder-free working electrode for highly effective electrocatalytic CO_2 reduction. By adjusting the surface morphology and chemical composition of CuO_x nanowires via surface reconstruction, large electrochemically active surface area and abundant Cu(+1) sites were generated, leading to remarkable activity for CO_2 electroreduction. The as-prepared hierarchical conductive electrode exhibited an enhanced Faradaic efficiency of 15.0% for ethanol formation ($FE_{C_2H_5OH}$) and a total Faradaic efficiency of 69.4% for all carbonaceous compounds ($FE_{C\text{-total}}$) at a mild applied potential of −0.45 V vs. RHE in 0.1 M $KHCO_3$ electrolyte. It achieved a 4-fold increase in $FE_{C\text{-total}}$ than that of Cu nanowire forest supported on 3D porous Cu foam (Cu-NWF@Cu-F) obtained by *in-situ* reduction of the CuO_x-NWF@Cu-F via annealing at H_2 atmosphere, and thereby effectively suppressed the hydrogen evolution side-reaction.

KEYWORDS

electrocatalytic CO_2 reduction, CuO_x nanowire forest 3D hierarchical nanostructure, surface reconstruction, enhanced carbonaceous product selectivity

1 Introduction

Industrial emission of carbon dioxide (CO_2), a major component of greenhouse gases, has been regarded as a leading cause of global warming. With the CO_2 concentration constantly increases in atmosphere, artificial CO_2 capture and conversion have become important to achieve a carbon-neutral energy cycle and to avoid climate catastrophe [1−3]. Among different CO_2 conversion approaches, electrocatalytic reduction of CO_2 into useful chemical feedstocks and hydrocarbon fuels has attracted lots of attention in the past decade [4, 5], due to the green process and convenient energy input by electricity [6−8]. However, since CO_2 is a thermodynamically stable molecule with the highest oxidation state of carbon, the cleavage of C=O bonds and the control of conversion products are difficult. Moreover, the electrocatalytic method is facing some critical challenges including high overpotential, low selectivity, and excessive energy consumption. To address these problems, various electrocatalysts have been explored in electrochemical CO_2 reduction, such as metal-organic complexes, metal/alloy nanostructures, metal oxides, metal chalcogenides, metal carbides and carbon materials, as summarized in our previous reviews [9, 10]. In particular, copper (Cu), as an earth-abundant metal, has been extensively employed for the production of carbonaceous compounds like CO [11, 12], HCOOH [13, 14] and value-added C_{2+} products [15−17]. In spite of the promising results from the previous studies, the selectivity and efficiency of Cu electrocatalyst are still to be improved, especially at low

Address correspondence to Bin Mu, bmu@asu.edu; Zuoxiu Tie, zxtie@nju.edu.cn; Zhong Jin, zhongjin@nju.edu.cn

applied potentials. More importantly, the working electrodes usually contain polymer binders and inactive materials, which may restrict the contact area between electrocatalyst and electrolyte, and thus decrease the overall catalytic activity [18].

In this work, a freestanding electrocatalyst composed of CuO_x nanowire forest *in-situ* grown on 3D porous Cu foam (CuO_x-NWF@Cu-F) was prepared and directly used as the working electrode in electrocatalytic CO_2 reduction without the need of any conductive additives or binders. Furthermore, fully reduced Cu-NWF@Cu-F electrode was obtained by the *in-situ* treatment of CuO_x-NWF@Cu-F under H_2 atmosphere. With the hierarchical structure, large electrochemical surface area and active Cu(+1) sites, the CuO_x-NWF@Cu-F electrode exhibited an highly improved Faradaic efficiency for ethanol formation ($FE_{C_2H_5OH}$) of 15.0% and a total Faradaic efficiency for all carbonaceous compounds ($FE_{C\text{-}total}$) of 69.4% at a mild potential of –0.45 V (vs. RHE) in 0.1 M $KHCO_3$ electrolyte. The $FE_{C\text{-}total}$ value of CuO_x-NWF@Cu-F electrode is four times higher than that of Cu-NWF@Cu-F (17.4%) and can effectively suppressed the hydrogen evolution reaction (HER). Moreover, this study provides further insight into the mechanism of catalytic activity in terms of the geometric effect and electronic structure of electrocatalysts.

2 Experimental

2.1 Preparation of CuO_x-NWF@Cu-F electrocatalyst

Firstly, the Cu-F was rinsed with acetone and immersed in 1.0 M diluted hydrochloric acid (HCl) aqueous solution for 10 min in order to remove the oxide layer on the Cu surface. Then, the Cu-F was ultrasonically cleaned with ethanol and deionized water in sequence. After dried with nitrogen gas, the cleaned Cu-F was immediately immersed into a mixed aqueous solution containing 0.133 M $(NH_4)_2S_2O_8$ and 2.667 M NaOH for different reaction times (10, 20 or 30 min). During this etching process, the surface of Cu-F gradually turned into deep blue, indicating the formation of $Cu(OH)_2$ nanowires. Then, the substrate was taken out from the reaction solution, and rinsed with deionized water and ethanol for several times. Subsequently, the substrate was annealed in a muffle furnace at 150 °C for 2 h under air atmosphere to obtain CuO_x-NWF@Cu-F with a color of dark brown.

2.2 Preparation of Cu-NWF@Cu-F electrocatalyst

The as-prepared CuO_x-NWF@Cu-F electrode was directly reduced in (5%) H_2/Ar atmosphere at 300 °C for 1 h to obtain the Cu-NWF@Cu-F electrode.

2.3 Characterizations

The nanoscale morphology and structure of samples were characterized by field-emission scanning electron microscopy (FESEM, JSM-6480) and transmission electron microscopy (TEM, JEM-2100). The crystal structures of products were determined by using a powder X-ray diffractometer (XRD, Bruker D8 Advance) with Cu Kα (λ = 1.5406 Å) irradiation in the range from 20° to 90° at a scanning rate of 10 °·min^{-1}. Raman signals were identified in the range of wavenumber between 50 and 700 cm^{-1} by a Horiba JY H800 Raman spectrometer. The oxidation states of Cu species before and after electrolysis were investigated by X-ray photoelectron spectroscopy (XPS, PHI-5000 Versa Probe X-ray photoelectron spectrometer) and X-ray-induced Cu LMM Auger spectroscopy with an Al Kα X-ray radiation. N_2 adsorption-desorption measurements were performed with an ASAP2020 HD88 instrument to determine the specific surface areas of samples.

2.4 CO_2 adsorption measurements

The CO_2 adsorption properties of the samples were analyzed on a Quantachrome Autosorb-IQ-2C-TCD-VP instrument. Prior to the adsorption experiments, the samples were degassed at 130 °C for 8 h. The CO_2 adsorption experiments proceeded at 25 °C stabilized by circulated water and with the testing pressure ranged from 0.05 to 1.00 bar.

2.5 Electrochemical measurements

All electrochemical measurements were carried out in a customized electrocatalysis instrument setup with a CHI-760E (CH Instrument, Shanghai, China) workstation. Briefly, 50 mL of 0.1 M $KHCO_3$ aqueous solution was used as the electrolyte in a closed electrochemical cell with a gas headspace of approximately 60 mL. After purged with CO_2 gas for 30 min, the electrolyte (with a pH value measured as ~6.8) was used to undergo electrochemical reduction of CO_2 in a conventional three-electrode system at ambient temperature (25 °C) and atmospheric pressure. A piece of selected Cu-based electrode was applied as working electrode. A platinum gauze electrode was used as counter electrode and saturated calomel electrode (SCE) was adopted as reference electrode. All the applied potentials (E) are shown in comparison with the potential of reversible hydrogen electrode (RHE) according to the following equation: E (vs. RHE) = E (vs. SCE) + 0.214 V + 0.059pH. To determine the electrochemical surface area (ECSA) and surface roughness factor (R_f), cyclic voltammetry (CV) method was employed to test the double layer capacitances of different samples. After the electrochemical reduction of samples in CO_2-saturated 0.1 M $KHCO_3$ solution at 0.45 V vs. RHE, CV experiments were performed in 0.1 M $HClO_4$ electrolyte within a potential range (–0.3 to –0.2 V vs. SCE) to ensure nonoccurrence of Faradaic processes. The selected scan rates were 10, 20, 30, 50, 80, 100 and 120 mV·s^{-1}, respectively. The slope of the linear regression was estimated from the CV curve with a plot of capacitive current density $\Delta j = (j_a - j_c)$ at –0.25 V vs. SCE against the scan rates, where j_a and j_c were the cathodic and anodic current densities, respectively. The value of slope was just double that of double-layer capacitance C_{dl}. The ECSA can be calculated from: ECSA = R_f*S, where S stands for the geometric area of the electrode. For the working electrode and the corresponding smooth metal electrode (assuming that the average C_{dl} of a smooth metal surface is 20 μF·cm^{-2}). R_f was calculated as: $R_f = C_{dl}$/20 μF·cm^{-2}. The Tafel slop for CO selectivity was calculated with a plot of the overpotential vs. the logarithm of the partial current density by means of linear sweep voltammetry (LSV) measurement and Faradaic efficiency of CO.

2.6 Quantitative analysis of the gaseous and liquid products

The generated gases were collected using a gastight syringe with a time interval of 60 min during the electrochemical reduction process of 4 h. Subsequently, the collected gas was directly injected into the gas sampling loop of a gas chromatograph (GC7900, Shanghai Techcomp) to periodically quantify the yield of gas products (n in moles). The different components in the gas product were detected by a thermal conductivity

detector (for H_2) and a flame ionization detector (for CO and hydrocarbons) with high-purity Ar flow as the carrier gas. The quantitative measurements were carried out two times to confirm the data accuracy. Liquid products generated from the CO_2 electrochemical reduction were measured and quantified by nuclear magnetic resonance technique (NMR, Bruker AV-600) after the overall electrocatalytic process of 4 h. The one-dimensional ^{1}H NMR spectra were measured with a necessary water pre-saturation method to suppress over water peak. With 0.1 mL of anhydrous dimethyl sulfoxide (DMSO, 99.5%, diluted to100 ppm (*v*/*v*) by water prior to use) as an internal standard, 0.6 mL of the electrolyte mixed with 0.1 mL of deuterated water (D_2O) was applied to determine the amounts of liquid products (*n* in moles). After confirming the electron number m needed to generate one gas/liquid molecule (CO, HCOOH, alcohols or hydrocarbons, etc.), the Faradaic efficiency can be calculated as follows: Faradaic efficiency (FE) = $mF^*n/Q = mF^*n/(I^*t)$, where *F* is the Faraday constant. The amount of transferred charge (*Q* in coulombs) to produce each product was calculated at a period of time (for gas products) or during the entire reaction time (for liquid products). $Q = I^*t$, where *I* (in amperes) is the constant current at a specific applied voltage and *t* is the time of electrolysis (in seconds) consumed for the corresponding reduction current.

3 Results and discussion

3.1 Synthesis and characterizations of CuO_x-NWF@Cu-F

The two-step preparation process of CuO_x-NWF@Cu-F electrode is illustrated in Fig. 1(a). After immersing the pristine Cu foam (Cu-F) in a mixed solution containing $(NH_4)_2S_2O_8$ and NaOH for 30 min, the color of Cu-F turned from orange to blue, and a forest of $Cu(OH)_2$ nanowires grown on Cu-F ($Cu(OH)_2$-NWF@Cu-F) was formed (Figs. S1(a) and S1(b) in the Electronic Supplementary Material (ESM)). After annealing under air, the $Cu(OH)_2$-NWF@Cu-F electrode was converted to CuO_x-NWF@Cu-F electrode. As indicated by the SEM image in Fig. 1(b), the CuO_x-NWF was densely covered on the surface of Cu-F. The length of CuO_x nanowires can reach tens of micrometers, and the average diameter is ~200 nm (Figs. 1(c) and 1(d)). Figures 1(e)–1(g) presents the TEM images of CuO_x-NWF@Cu-F electrode. A highly rough and nanoporous surface was achieved, which could expose abundant active sites to promote the activity of CO_2 electro-reduction (Figs. 1(e) and 1(f)). High-resolution TEM (HRTEM) image in Fig. 1(g) demonstrates that the CuO_x nanowires are composed of numerous of highly crystalline grains. The measured lattice distances of 0.247 and 0.240 nm can be assigned to the $(\bar{1}11)$ planes of CuO and the (111) planes of Cu_2O, respectively. Meanwhile, the corresponding selected area electron diffraction (SAED) pattern in the inset of Fig. 1(g) confirms the highly crystalline nature of CuO_x nanowires.

By adjusting the reaction duration, different CuO_x-NWF@Cu-F samples with tunable lengths and densities were also prepared. Figures S1 and S2(a) in the ESM show the SEM images and optical images of CuO_x-NWF@Cu-F samples achieved with different soaking durations, respectively. The CuO_x-NWF@Cu-F samples prepared with the shorten soaking duration of 10 and 20 min are denoted as CuO_x-NWF@Cu-F (10 min) and CuO_x-NWF@Cu-F (20 min), respectively. As shown in Figs. S1(c)–S1(f) in the ESM, with the soaking time decreased, the control samples of CuO_x-NWF@Cu-F (10 min) and CuO_x-NWF@Cu-F (20 min) still show the similar morphology to that of CuO_x-NWF@Cu-F, but the length and density of CuO_x nanowires are decreased. The high crystallinity of different

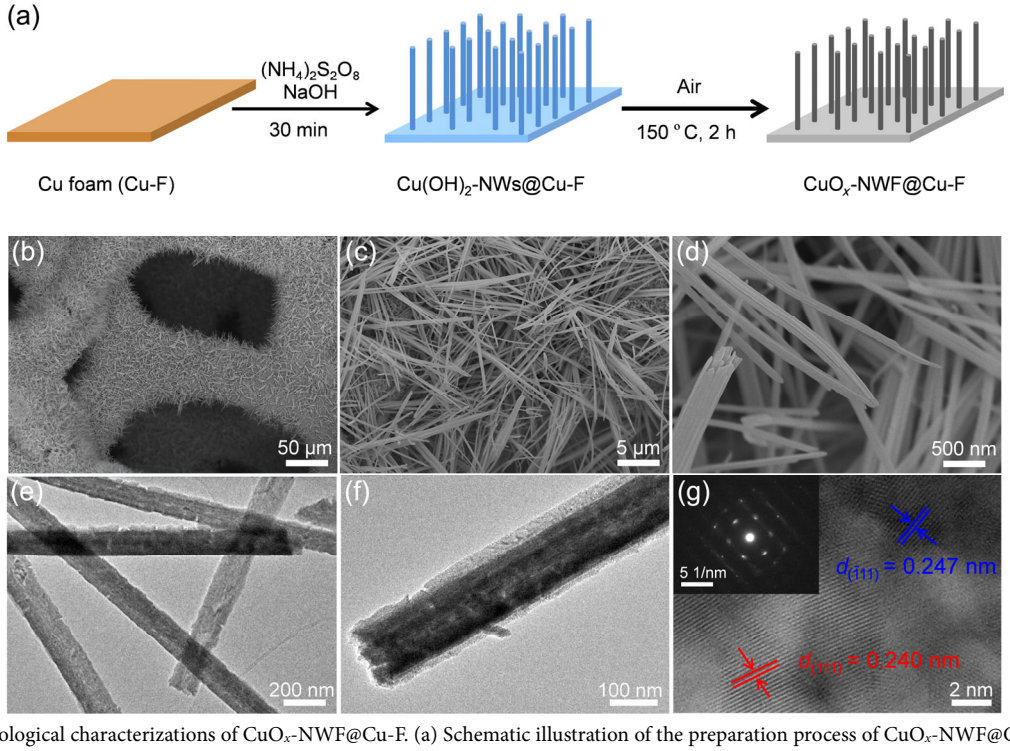

Figure 1 Morphological characterizations of CuO_x-NWF@Cu-F. (a) Schematic illustration of the preparation process of CuO_x-NWF@Cu-F. (b)–(d) SEM images of CuO_x-NWF@Cu-F at different magnifications. TEM ((e) and (f)) and HRTEM (g) images of as-prepared CuO_x nanowires. The lattice fringes in (g) are assigned to the $(\bar{1}11)$ planes of CuO and (111) planes of Cu_2O, respectively. The corresponding SAED pattern in the insert of (g) reveals the crystalline nature of as-prepared CuO_x nanowires.

samples was further confirmed by XRD spectra, as presented in Figs. S2(b) and S2(c) in the ESM. The XRD pattern of pristine Cu-F was indexed to JCPDS card No. 03-1005. In Fig. S2(c) in the ESM, the magnified spectra in the range of 10°–70° were attributed to CuO_x-NWF@Cu-F (JCPDS card No. 03-0867 and No. 03-0898) and $Cu(OH)_2$-NWs@Cu-F (JCPDS card No. 03-0310), respectively. Moreover, according to the Raman spectrum of CuO_x-NWF@Cu-F in Fig. S2(d) in the ESM, the peaks at 97, 147 and 217 cm^{-1} confirmed the presence of Cu_2O species and the peak at 629 cm^{-1} are assigned to CuO species.

3.2 Electrocatalytic CO_2 performance of CuO_x-NWF@Cu-F and Cu-NWF@Cu-F

To measure the electrocatalytic activity of the samples for CO_2 reduction, electrochemical tests were carried out in a customized electrochemical cell (Scheme S1 in the ESM). The self-designed electrochemical cell was divided into cathode and anode compartments by proton exchange membrane, preventing the oxidation of products during CO_2 reduction reaction. As shown in Fig. 2(a), the CuO_x-NWF@Cu-F electrode exhibited a sharp variation of current density during the initial 20 min, indicating the change of surface states via electrochemical reduction at an applied negative voltage. Figure S2(a) in the ESM visually showed the color change of CuO_x-NWF@Cu-F before and after 20-min electrolysis of CO_2 reduction. To deeply investigate the variation of chemical compositions on the surface of electrocatalyst before and after electrolysis, XPS were carried out (Figs. 2(b)−2(d)). In O 1s region (Fig. 2(c)), the characteristic peaks of lattice oxygen of Cu_2O and CuO ($O_L(Cu^+)$ and $O_L(Cu^{2+})$), oxygen vacancy (O_V) and adsorbed oxygen (O_C) indicate the coexistence of Cu_2O and CuO on the surface of CuO_x-NWF (before electrolysis). In Fig. 2(d), there are distinct differences in Cu 2p region of CuO_x-NWF@Cu-F before and after electrolysis. The Cu(II) peaks (955.4 and 935.5 eV) and Cu^{2+} satellite (Cu^{2+} sat.) peaks appeared in the XPS spectrum of CuO_x-NWF@Cu-F (before electrolysis). This further declare the presence of CuO on the surface of CuO_x-NWF@Cu-F (before electrolysis). In comparison, the CuO_x-NWF@Cu-F (after electrolysis) only shows two main peaks at 952.2 and 932.4 eV, which are assigned to Cu^{1+}/Cu^0 states. Meanwhile, the peaks of CuO_x-NWF@Cu-F (after electrolysis) related to Cu^{2+} sat. are almost disappeared [19, 20], indicating that almost all of Cu^{2+} species are reduced during the electrolysis and the Cu^{1+}/Cu^0 species in CuO_x-NWF are substantially responsible for the electrochemical activity in the entire CO_2 electro-reduction process. Combined with X-ray-induced Cu LMM Auger studies (Fig. S3 in the ESM), these results reveal that the surface of CuO_x-NWF@Cu-F is mainly composed of Cu^{1+} species, while the presence of Cu^0 species is might due to the weak signal peak of Cu-F substrate.

To reveal the CO_2 electrocatalytic activity of CuO_x-NWF@Cu-F electrode, the LSV curve, current density and Faradaic efficiencies (FE) of the products during CO_2 electro-reduction have been investigated. In Fig. S4 in the ESM, the CuO_x-NWF@Cu-F in CO_2-saturated electrolyte exhibits higher current densities than in N_2-saturated electrolyte, indicating that CuO_x-NWF@Cu-F prefers to catalyze CO_2 reduction rather than hydrogen evolution. As shown in Fig. 2(a), when the applied potential is varied from −0.35 to −0.75 V (vs. RHE), an enhanced current density is achieved at a more negative potential, and the current value shows negligible decrease as the time goes by. As shown in the SEM images (Figs. S5(a)−S5(c) and S6(b) and S6(c) in the ESM), the nanowire-like morphology of CuO_x-NWF before and after CO_2 electroreduction has no significant change. Meanwhile, in comparison of XRD pattern before and after electro-reduction (Fig. S6(a) in the ESM), the main peaks attributed to Cu species still existed after electrolysis, which indicate the stability of crystalline phase

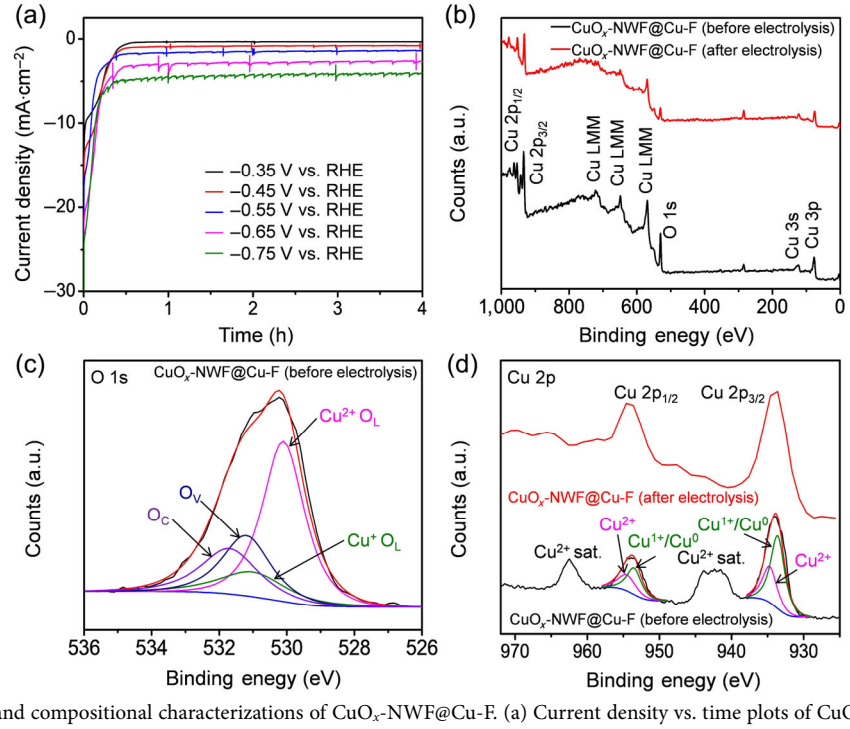

Figure 2 The structural and compositional characterizations of CuO_x-NWF@Cu-F. (a) Current density vs. time plots of CuO_x-NWF@Cu-F electrode at different applied potentials from −0.35 to −0.75 V (vs. RHE) during CO_2 electroreduction. (b) XPS spectra of CuO_x-NWF@Cu-F electrode before and after 20-min electrolysis of CO_2 reduction. (c) O 1s XPS spectrum of CuO_x-NWF@Cu-F before electrolysis. (d) Cu 2p XPS spectra of CuO_x-NWF@Cu-F before and after 20-min electrolysis of CO_2 reduction, respectively.

during the electro-reduction process. As shown in Fig. 3(a), besides CO and H_2 gases, a quantity of liquid products was detected (Fig. S7 and Table S1 in the ESM), and the $FE_{C_2H_5OH}$ reached more than 15.0%. Meanwhile, the highest $FE_{C\text{-total}}$ was 69.4% and the total Faradaic efficiency for all products was up to 98.6% at an applied potential of –0.45 V vs. RHE. Since the HER acts as a main competitive reaction during CO_2 reduction electrolysis, H_2 was also determined and quantified as a by-product. At relatively negative potentials lower than –0.45 V vs. RHE, the yield of H_2 by-product increased, which indicated that the more negative applied potential was more favorable for the HER rather than driving CO_2 reduction. At a more negative potential, the obvious diminish of $FE_{C\text{-total}}$ and the elevated H_2 evolution indicated the CO_2 mass transport limitations at higher current density [12]. As catalytic stability is an essential parameter to evaluate the performance of an electrocatalyst, the long-term catalytic performance of CuO_x-NWF@Cu-F has been evaluated, and no obvious degradation was observed in consecutive test over 24 h (Fig. S8 in the ESM).

Since the CuO_x-NWF@Cu-F electrode exhibited preferable electrocatalytic activity for CO_2 conversion, the performances of Cu-NWF@Cu-F electrode with reduced Cu nanowires were also compared to reveal the structure sensitivity towards the electrocatalytic activity [11, 21, 22]. The Cu nanowires on the Cu-NWF@Cu-F electrode were directly obtained from the CuO_x-NWF@Cu-F electrode by annealing in H_2 atmosphere at 300 °C, which was used as a control sample towards CO_2 electro-reduction. As shown in Fig. S9 in the ESM and Fig. 3(d), even if the total current densities reached high values, the Cu-NWF@Cu-F electrode still showed inferior Faradaic efficiencies of carbonaceous compounds to those of CuO_x-NWF@Cu-F electrode. This indicated that H_2 was the dominant product on the Cu-NWF@Cu-F electrode. Compared with CuO_x-NWF@Cu-F, the Cu-NWF@Cu-F electrode exhibited smaller electrochemical surface area (ECSA), suggesting its less exposed active sites towards CO_2 adsorption (Figs. S10(a)–S10(c) and S11 in the ESM). Observed from the SEM and XRD characterizations (Figs. S5(d)–S5(f) and S6(d)–S6(f) in the ESM), the Cu-NWF@Cu-F electrode after electrochemical CO_2 reduction exhibited dilapidated surface morphology and decreased crystallinity, which revealed its undesirable structure stability.

Due to the considerable electroreduction activity differences between CuO_x-NWF@Cu-F and Cu-NWF@Cu-F, the surface structures of these two electrodes were further compared to essentially explain the enhanced performances of CuO_x-NWF@Cu-F towards CO_2 electro-reduction. TEM and HRTEM characterizations clearly indicated different active planes were formed on these two electrodes through different synthetic approaches. As presented in Figs. 3(b) and 3(c), the Cu_2O (111) planes were favorably emerged from the CuO_x-NWF@Cu-F sample, while the fully reduced Cu-NWF@Cu-F sample preferably exposed the Cu (111) planes (Figs. 3(e) and 3(f)) [23]. As evidenced by previous DFT calculations [24, 25], the exposed Cu_2O(111) facets and Cu(+1) sites tended to display stronger bonding capability for $CO_2^{\cdot-}$ intermediates and optimal adsorbed energy for CO* intermediates, thus leading to high selectivity towards carbonaceous compounds and effective suppression of the HER. These results further verify that the surface structures of Cu-based nanomaterials can great affect the activity and selectivity of electrochemical CO_2 reaction. To make clear comparisons, the representative research works on other Cu-based electrodes in previous literature were listed in Table S2 in the ESM [12, 13, 19, 21, 26–30]. Among those Cu-based catalysts studied thus far, CO_2 can be selectively converted to CO, HCOOH, or more importantly, to ethanol, with relatively high faradaic efficiencies via different pathways. The comparative result suggests the competitive carbonaceous product selectivities realized in this work. This indicates

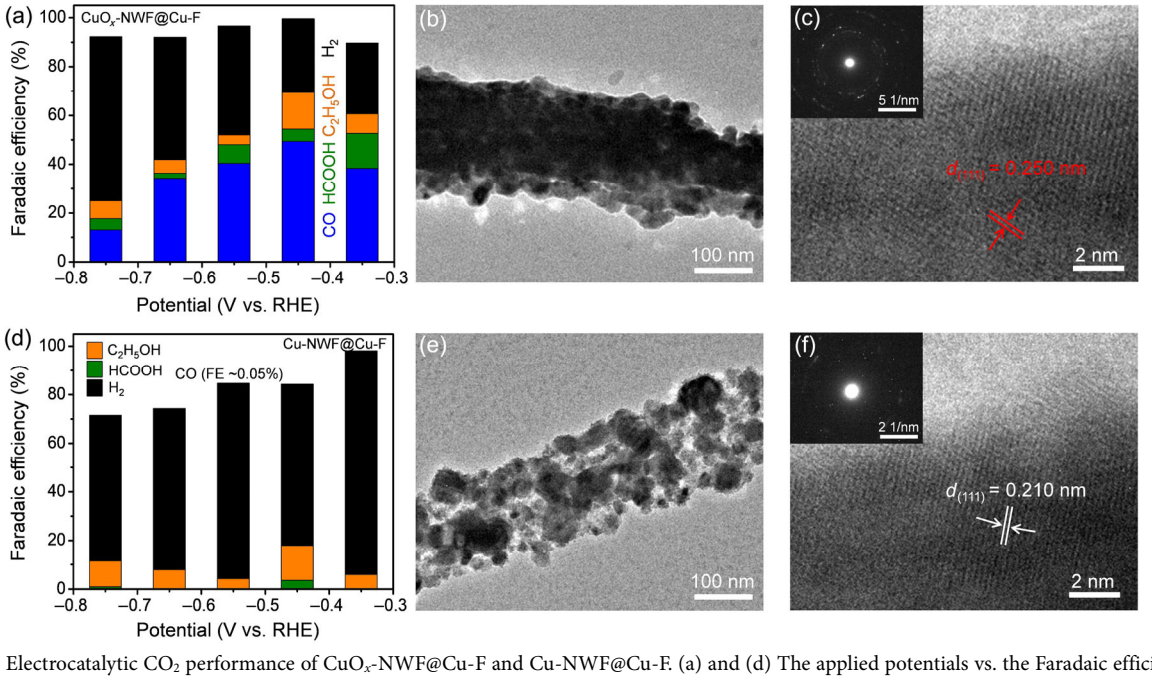

Figure 3 Electrocatalytic CO_2 performance of CuO_x-NWF@Cu-F and Cu-NWF@Cu-F. (a) and (d) The applied potentials vs. the Faradaic efficiencies of major products for (a) CuO_x-NWF@Cu-F and (d) Cu-NWF@Cu-F during electrocatalytic CO_2 reduction. (b) and (c) HRTEM images of CuO_x-NWF@Cu-F (after electrolysis) with the lattice fringes assigned to the (111) planes of Cu_2O. (e) and (f) HRTEM images of Cu-NWF@Cu-F with the lattice fringes assigned to the (111) facets of Cu. The corresponding SAED patterns in the inserts of (c) and (f) indicate the crystalline nature of CuO_x-NWF@Cu-F and Cu-NWF@Cu-F.

that the rational design and modulation of surface species of Cu-based electrocatalysts is of great importance for further improving the electrocatalytic activity and selectivity towards electrochemical CO_2 reduction.

3.3 Electrocatalytic CO_2 performance of CuO_x-NWF@Cu-F with different growth time

To understand the importance of morphology and surface structure on the activity for CO_2 electro-reduction, we also performed extra contrast experiments to determine the optimal length and density of CuO_x-NWF. It is worth noting that the CuO_x-NWF grew longer and denser as the growth time increases. As shown in Figs. 3(a), 4(d)–4(g), the CuO_x-NWF@Cu-F electrode (with the default growth time of 30 min) exhibited the optimal electrochemical CO_2 reduction activity, highest current density and suppressed H_2 evolution when compared with those of pristine Cu-F, CuO_x-NWF@Cu-F (10 min) and CuO_x-NWF@Cu-F (20 min). Moreover, the CuO_x-NWF@Cu-F electrode only required an overpotential of less than 100 mV to reach the optimal $FE_{C\text{-}total}$. As presented in Figs. 4(h) and 4(i), with longer growth time of Cu nanowires, CO product was more likely to be generated at a mild applied potential accompanied with higher partial current density for CO production (j_{CO}). Notably, the drop of Faradaic efficiencies for CO production (FE_{CO}) at high current densities was not only because of the mass transport limitation, but also because CO molecules could be further reduced to the C_{2+} liquid products (like C_2H_5OH) [11]. Among the samples, the pristine Cu-F was the least active one for CO_2 electroreduction, since H_2 was the dominant product for pristine Cu-F. Moreover, the rate-determining steps for CO_2 electro-reduction were revealed by the calculated Tafel slops (Fig. S12 in the ESM). The Tafel slope for CO production obtained on CuO_x-NWF@Cu-F electrode was approximately 116 mV per decade. This result suggested a rate-determining step involving initial one electron transfer for the formation of surface adsorbed $CO_2^{\cdot-}$ intermediate. When compared with pristine Cu-F (221.7 mV per decade), the smaller Tafel slop of CuO_x-NWF@Cu-F indicates its faster reaction kinetics for CO_2 reduction. The improved CO_2 reduction activity of CuO_x-NWF@Cu-F was attributed to the surface reconstruction derived from *in-situ* grown CuO_x-NWF. The aforementioned results indicate that the role of Cu-F itself was insignificant for the electrocatalytic activity of CuO_x-NWF@Cu-F. The essential characterizations and electrochemical test results further explain the optimal activity of CuO_x-NWF@Cu-F with the highest growth time of 30 min toward CO_2 electrocatalysis. When compared to other CuO_x-NWF@Cu-F electrodes with different lengths and densities of CuO_x nanowires, the highest ECSA and largest specific surface area of CuO_x-NWF@Cu-F electrode with the growth time of 30 min (Figs. S10 and S13 in the ESM) suggest the more abundant low-coordination active sites, which was responsible for its enhanced electrocatalytic performance. Moreover, as shown in Fig. S11 in the ESM, the largest CO_2

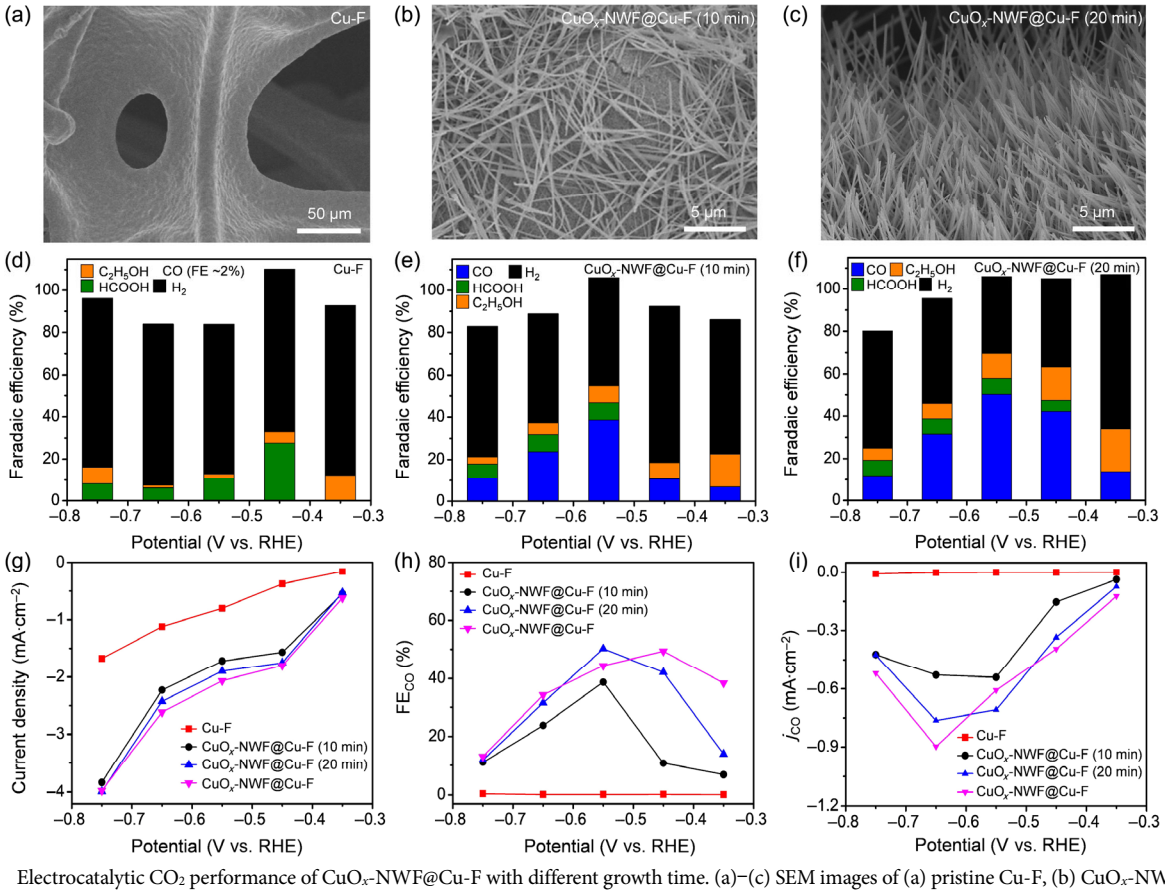

Figure 4 Electrocatalytic CO_2 performance of CuO_x-NWF@Cu-F with different growth time. (a)−(c) SEM images of (a) pristine Cu-F, (b) CuO_x-NWF@Cu-F (10 min) and (c) CuO_x-NWF@Cu-F (20 min). (d)−(f) The applied potentials vs. Faradaic efficiencies of the major products of (d) pristine Cu-F, (e) CuO_x-NWF@Cu-F (10 min) and (f) CuO_x-NWF@Cu-F (20 min). (g)−(i) The applied potentials vs. total current densities, (h) Faradaic efficiencies for CO production (FE_{CO}) and (i) partial current densities for CO production (j_{CO}) of pristine Cu-F, CuO_x-NWF@Cu-F (10 min), CuO_x-NWF@Cu-F (20 min) and CuO_x-NWF@Cu-F with different growth durations for electrocatalytic CO_2 reduction.

uptake capacity of the CuO_x-NWF@Cu-F electrode further facilitates CO_2 electroreduction.

3.4 Electrochemical reaction mechanism

To further explore the formation mechanism of different carbonaceous products generated on CuO_x-NWF@Cu-F electrode during electrocatalytic CO_2 reduction, the reaction pathway was proposed in Fig. 5. The formation of $CO_2^{\cdot-}$ intermediate by the first electron transfer demands a more negative potential than the following chemical reaction steps, therefore it generally acts as the rate determining step in CO_2 electrocatalysis. Two crucial factors, including the strong binding of $CO_2^{\cdot-}$ intermediate and the improved *CO binding capability on the active sites of CuO_x-NWF, are attributed to the enhanced selectivity of carbonaceous products. Meanwhile, a small quantity of $HCOO^-$ product has also emerged at less negative potentials because of the relatively weak bonding of $CO_2^{\cdot-}$ intermediate on the surface of CuO_x-NWF. Ethanol, a higher energy-density hydrocarbon product prefers to generate through the CH_3CH_2O* intermediate from the dimerization of two *CO intermediates due to the strong binding capability and high cover density of *CO intermediates on the surface of CuO_x-NWF. As a result, the CuO_x-NWF@Cu-F electrode realizes enhanced electrocatalytic selectivity and relatively low overpotential toward CO_2 electro-reduction of via effective surface reconstruction.

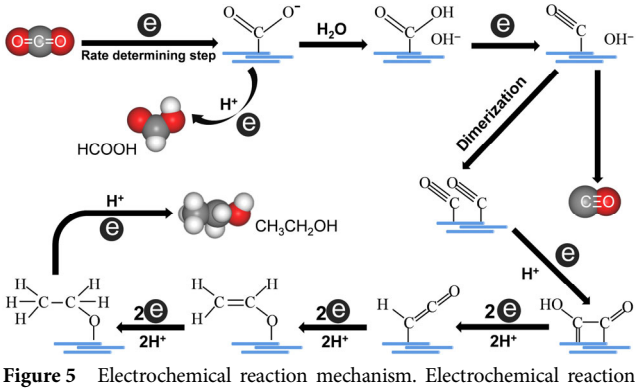

Figure 5 Electrochemical reaction mechanism. Electrochemical reaction mechanism for the formation of carbonaceous compounds on CuO_x-NWF@Cu-F electrode during electrocatalytic CO_2 reduction.

4 Conclusion

In summary, we report the *in-situ* formation of a 3D hierarchical and free-standing CuO_x-NWF@Cu-F electrocatalyst through a convenient two-step preparation process. The as-obtained CuO_x-NWF@Cu-F electrode could reach an optimal $FE_{C_2H_5OH}$ of 15.0% and a corresponding $FE_{C\text{-total}}$ of 69.4% at −0.45 V (vs. RHE), which effectively suppress the HER as a side reaction. Owing to the high ECSA of Cu nanowire arrays, the CuO_x-NWF@Cu-F electrode could provide smooth electron transport and abundant active sites to improve CO_2 adsorption. Moreover, owing to the lowly coordinated and electrochemically active Cu(+1) sites, $CO_2^{\cdot-}$ intermediates were preferably stabilized to the active sites of CuO_x-NWF@Cu-F to achieve improved CO_2 reduction selectivity towards carbonous compounds, especially ethanol as a main product in liquid phase. This work suggests a convenient and feasible strategy to enhance the selectivity of electrochemical CO_2 reduction by tuning the geometric factors and electronic structures of Cu-based electrocatalysts, which provided a broad platform for the design of advanced electrocatalysts towards carbon peaking and carbon neutrality.

Acknowledgements

Author contributions

Z. J. and W. J. Z. conceived the idea of this study and designed the experiments. W. J. Z. performed the sample synthesis, characterizations and electrocatalytic measurements. M. H. J., S. Y. Y., and H. Y. performed the material characterizations. B. M. and Z. X. T. helped the data analysis. W. J. Z. and Z. J. co-wrote and revised the manuscript. All the authors discussed the results. Z. J. supervised this research project.

Funding Sources

The authors are grateful to the supports from the National Key R&D Program of China (No. 2017YFA0208200), the National Natural Science Foundation of China (Nos. 22022505 and 21872069), the Fundamental Research Funds for the Central Universities (Nos. 020514380266, 020514380272 and 020514380274), the Scientific and Technological Innovation Special Fund for Carbon Peak and Carbon Neutrality of Jiangsu Province (No. BK20220008), the Nanjing International Collaboration Research Program (Nos. 202201007 and 2022SX00000955), and the Suzhou Gusu Leading Talent Program of Science and Technology Innovation and Entrepreneurship in Wujiang District (No. ZXL2021273).

Electronic Supplementary Material: Supplementary material (SEM images, XRD patterns, Raman spectra, NMR spectra, CO_2 adsorption isotherms and electrochemical parameters) is available in the online version of this article at https://doi.org/10.26599/NRE.2022.9120033.

Declaration of conflicting interests

The authors declare no conflicting interests regarding the content of this article.

References

[1] Centi, G.; Quadrelli, E. A.; Perathoner, S. Catalysis for CO_2 conversion: A key technology for rapid introduction of renewable energy in the value chain of chemical industries. *Energy Environ. Sci*. **2013**, *6*, 1711–1731.

[2] Song, C. S. Global challenges and strategies for control, conversion and utilization of CO_2 for sustainable development involving energy, catalysis, adsorption and chemical processing. *Catal. Today* **2006**, *115*, 2–32.

[3] Ozin, G. A. Throwing new light on the reduction of CO_2. *Adv. Mater.* **2015**, *27*, 1957–1963.

[4] Qiao, J. L.; Liu, Y. Y.; Hong, F.; Zhang, J. J. A review of catalysts for the electroreduction of carbon dioxide to produce low-carbon fuels. *Chem. Soc. Rev*. **2014**, *43*, 631–675.

[5] Yang, Y.; Ajmal, S.; Zheng, X. Z.; Zhang, L. W. Efficient nanomaterials for harvesting clean fuels from electrochemical and photoelectrochemical CO_2 reduction. *Sustainable Energy Fuels* **2018**, *2*, 510–537.

[6] Khan, J.; Arsalan, M. H. Solar power technologies for sustainable electricity generation-A review. *Renew. Sust. Energy Rev*. **2016**, *55*, 414–425.

[7] Yang, J.; Chen, B. Emergy-based sustainability evaluation of wind power generation systems. *Appl. Energy* **2016**, *177*, 239–246.

[8] Zhou, Y.; Hejazi, M.; Smith, S.; Edmonds, J.; Li, H.; Clarke, L.;

Calvin, K.; Thomson, A. A comprehensive view of global potential for hydro-generated electricity. *Energy Environ. Sci.* **2015**, *8*, 2622–2633.
[9] Zhang, W. J.; Hu, Y.; Ma, L. B.; Zhu, G. Y.; Wang, Y. R.; Xue, X. L.; Chen, R. P.; Yang, S. Y.; Jin, Z. Progress and perspective of electrocatalytic CO_2 reduction for renewable carbonaceous fuels and chemicals. *Adv. Sci.* **2018**, *5*, 1700275.
[10] Zhang, W. J.; Jin, Z.; Chen, Z. P. Rational-designed principles for electrochemical and photoelectrochemical upgrading of CO_2 to value-added chemicals. *Adv. Sci.* **2022**, *9*, 2105204.
[11] Raciti, D.; Livi, K. J.; Wang, C. Highly dense Cu nanowires for low-overpotential CO_2 reduction. *Nano Lett.* **2015**, *15*, 6829–6835.
[12] Ma, M.; Djanashvili, K.; Smith, W. A. Selective electrochemical reduction of CO_2 to CO on CuO-derived Cu nanowires. *Phys. Chem. Chem. Phys.* **2015**, *17*, 20861–20867.
[13] Chung, J.; Won, D. H.; Koh, J.; Kim, E. H.; Woo, S. I. Hierarchical Cu pillar electrodes for electrochemical CO_2 reduction to formic acid with low overpotential. *Phys. Chem. Chem. Phys.* **2016**, *18*, 6252–6258.
[14] Guo, S. J.; Zhao, S. Q.; Gao, J.; Zhu, C.; Wu, X. Q.; Fu, Y. J.; Huang, H.; Liu, Y.; Kang, Z. H. Cu-C dots nanocorals as electrocatalyst for highly efficient CO_2 reduction to formate. *Nanoscale* **2017**, *9*, 298–304.
[15] Loiudice, A.; Lobaccaro, P.; Kamali, E. A.; Thao, T.; Huang, B. H.; Ager, J. W.; Buonsanti, R. Tailoring copper nanocrystals towards C_2 products in electrochemical CO_2 reduction. *Angew. Chem., Int. Ed.* **2016**, *55*, 5789–5792.
[16] Roberts, F. S.; Kuhl, K. P.; Nilsson, A. High selectivity for ethylene from carbon dioxide reduction over copper nanocube electrocatalysts. *Angew. Chem., Int. Ed.* **2015**, *54*, 5179–5182.
[17] Manthiram, K.; Beberwyck, B. J.; Alivisatos, A. P. Enhanced electrochemical methanation of carbon dioxide with a dispersible nanoscale copper catalyst. *J. Am. Chem. Soc.* **2014**, *136*, 13319–13325.
[18] Wang, H.; Jia, J.; Song, P. F.; Wang, Q.; Li, D. B.; Min, S. X.; Qian, C. X.; Wang, L.; Li, Y. F.; Ma, C. et al. Efficient electrocatalytic reduction of CO_2 by nitrogen-doped nanoporous carbon/carbon nanotube membranes: A step towards the electrochemical CO_2 refinery. *Angew. Chem., Int. Ed.* **2017**, *56*, 7847–7852.
[19] Tang, W.; Peterson, A. A.; Varela, A. S.; Jovanov, Z. P.; Bech, L.; Durand, W. J.; Dahl, S.; Nørskov, J. K.; Chorkendorff, I. The importance of surface morphology in controlling the selectivity of polycrystalline copper for CO_2 electroreduction. *Phys. Chem. Chem. Phys.* **2012**, *14*, 76–81.
[20] Li, Q.; Fu, J. J.; Zhu, W. L.; Chen, Z. Z.; Shen, B.; Wu, L. H.; Xi, Z.; Wang, T. Y.; Lu, G.; Zhu, J. J. et al. Tuning Sn-catalysis for electrochemical reduction of CO_2 to CO via the core/shell Cu/SnO_2 structure. *J. Am. Chem. Soc.* **2017**, *139*, 4290–4293.
[21] Ma, M.; Djanashvili, K.; Smith, W. A. Controllable hydrocarbon formation from the electrochemical reduction of CO_2 over Cu nanowire arrays. *Angew. Chem., Int. Ed.* **2016**, *55*, 6680–6684.
[22] Li, Y. F.; Cui, F.; Ross, M. B.; Kim, D.; Sun, Y. C.; Yang, P. D.; Structure-sensitive CO_2 electroreduction to hydrocarbons on ultrathin 5-fold twinned copper nanowires. *Nano Lett.* **2017**, *17*, 1312–1317.
[23] Rashid, N. M.; Kishi, N.; Soga, T. Effects of reduction temperature on copper nanowires growth by thermal reduction of copper oxide nanowires. *Mod. Phys. Lett. B* **2016**, *30*, 1650193.
[24] Song, S. Z.; Meng, J.; Wang, Y.; Zhou, J.; Zhang, L. J.; Gao, N.; Guan, C. Z.; Xiao, G. P.; Hu, Z. W.; Lin, H. J. et al. Molten salt treated Cu foam catalyst for selective electrochemical CO_2 reduction reaction. *ChemistrySelect* **2020**, *5*, 11927–11933.
[25] Möller, T.; Scholten, F.; Thanh, T. N.; Sinev, I.; Timoshenko, J.; Wang, X. L.; Jovanov, Z.; Gliech, M.; Cuenya, B. R.; Varela, A. S. et al. Electrocatalytic CO_2 reduction on CuO_x nanocubes: Tracking the evolution of chemical state, geometric structure, and catalytic selectivity using operando spectroscopy. *Angew. Chem., Int. Ed.* **2020**, *59*, 17974–17983.
[26] Li, C. W.; Kanan, M. W. CO_2 reduction at low overpotential on Cu electrodes resulting from the reduction of thick Cu_2O films. *J. Am. Chem. Soc.* **2012**, *134*, 7231–7234.
[27] Dutta, A.; Rahaman, M.; Luedi, N. C.; Mohos, M.; Broekmann, P. Morphology matters: Tuning the product distribution of CO_2 electroreduction on oxide-derived Cu foam catalysts. *ACS Catal.* **2016**, *6*, 3804–3814.
[28] Larrazábal, G. O.; Martín, A. J.; Krumeich, F.; Hauert, R.; Pérez-Ramírez, J. Solvothermally-prepared Cu_2O electrocatalysts for CO_2 reduction with tunable selectivity by the introduction of p-block elements. *ChemSusChem* **2017**, *10*, 1255–1265.
[29] Kim, D.; Resasco, J.; Yu, Y.; Asiri, A. M.; Yang, P. D. Synergistic geometric and electronic effects for electrochemical reduction of carbon dioxide using gold-copper bimetallic nanoparticles. *Nat. Commun.* **2014**, *5*, 4948.
[30] Choi, J.; Kim, M. J.; Ahn, S. H.; Choi, I.; Jang, J. H.; Ham, Y. S.; Kim, J. J.; Kim, S. K. Electrochemical CO_2 reduction to CO on dendritic Ag-Cu electrocatalysts prepared by electrodeposition. *Chem. Eng. J.* **2016**, *299*, 37–44.

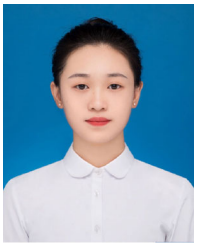

Wenjun Zhang received her Ph.D. degree under the supervision of Prof. Zhong Jin in the School of Chemistry and Chemical Engineering, Nanjing University, P. R. China. Since 2020, she has worked in the College of Chemical Engineering, Nanjing Forestry University (China). Her main interest is the design and fabrication of nano-catalysts for electrochemical reduction of carbon dioxide and catalytic conversion of biomass.

Prof. Zhong Jin received his B.S. (2003) and Ph.D. (2008) in chemistry from Peking University. He worked as a postdoctoral scholar at Rice University and Massachusetts Institute of Technology. Now he is a professor in School of Chemistry and Chemical Engineering at Nanjing University. He leads a research group working on functional nanomaterials and devices for energy conversion and storage.